Fusion and back-angle quasielastic measurements in ^{30}Si $+$ ^{156}Gd near the Coulomb barrier

Rinku Prajapat [1,*] Moumita Maiti [1,†] Rishabh Kumar,[1] Malvika Sagwal,[1] Gonika ,[2] Chandra Kumar,[2] Rohan Biswas,[2]
J. Gehlot,[2] S. Nath,[2] and N. Madhavan[2]

[1]*Department of Physics, Indian Institute of Technology Roorkee, Roorkee-247667 Uttarakhand, India*
[2]*Nuclear Physics Group, Inter-University Accelerator Centre, New Delhi-110067, India*

Background: Advancement in accelerator facilities has opened the door to dig deep to understand the interplay between nuclear reactions and structures. Although the influence of inelastic excitations on nuclear scattering and sub-barrier fusion is somewhat established, a clear understanding of nucleon transfer with a positive-Q value is yet to achieve.

Purpose: The objective of this paper is to examine the role of the $2n$-transfer channel with a positive Q value on sub-barrier fusion and back-angle quasielastic (QE) scattering in the ^{30}Si $+$ ^{156}Gd reaction. Furthermore, extraction of barrier distributions (BDs) from fusion and QE scattering to infer their shapes is also a prime goal.

Method: The excitation functions (EFs) of fusion and back-angle QE scattering have been measured over a wide range of incident beam energy around the Coulomb barrier using a recoil mass spectrometer. Furthermore, BDs have been extracted using the measured fusion and back-scattered QE data. The underlying findings have been analyzed within the framework of coupled-channel (CC) formalism using CCFULL and ECC programs.

Results: Fusion enhancement has been observed compared to those predicted from the one-dimensional barrier penetration model at sub-barrier energies. Fusion enhancement and QE EFs are explained by CC predictions considering the collective excitations among the colliding nuclei. The inclusion of $2n$ transfer and collective excitations in CCFULL improves the fit to the experimental fusion data in a short span of energy window around the Coulomb barrier, whereas no significant effect has been observed at the sub-barrier region. However, no such effect of $2n$-pickup transfer has been observed from ECC model calculations. Thus, no firm conclusion can be made on the role of $2n$-pickup transfer with a positive Q value in present measurements.

Conclusion: Fusion EFs have been successfully explained by the CC calculations using CCFULL and ECC model codes. No significant effect of the $2n$-pickup channel with a positive Q value was observed on sub-barrier fusion enhancement. However, QE EFs are reproduced by considering the collective excitations and $2n$-transfer channel couplings. Fusion and QE BDs are similar in shape within the experimental uncertainty. One-dimensional barrier parameters extracted from the measured data agree with the different theoretical models. Also, the present system obeys the systematic based on deformation values after transfer at the exit.

I. INTRODUCTION

Heavy-ion fusion and multinucleon-transfer reactions are the essential routes for the production of exotic nuclei with an appropriate choice of highly effective and selective separators, state-of-the-art detectors, and sizable primary beam intensities to extend the nuclear landscape [1,2]. Even the fusion of light nuclei is also a source of energy generation in stars, stellar nucleosynthesis, and primordial nucleosynthesis [3]. The sub-barrier fusion in heavy-ion ($A \geqslant 4$) collisions demonstrates the richness of detailed information concerning the nuclear structure effects of the colliding nuclei. Thus, it ignites the mind of researchers to probe the reason for the observed enhancement of cross section in sub-barrier fusion. In recent years, various experiments, theoretical models, and

potentials have been available to understand one or the other aspects of fusion dynamics and scattering.

Efforts have also been made to interpret sub-barrier fusion enhancement relative to the one-dimensional barrier penetration model (1D-BPM) [4–14] from early days. Among them, coupled channel (CC) calculations with different degrees of freedom, such as couplings to inelastic excitations [8,9], static deformations [10,11], zero-point oscillations [6], etc., have already been inferred. However, the influence of neutron transfer channels especially with positive Q values is yet to understand owing to multifold reasons, for instance, the difficulty in consideration of transfer channels in the total coupled channel Schrödinger equations explicitly, segregation of the transfer channel effect from the impact of other collective properties of colliding nuclei in sub-barrier fusion, etc. [15,16]. Recently, Zagrebaev [17] proposed the empirical channel coupling (ECC) approach that is capable of considering positive Q-value multineutron rearrangement (transfer) channels in the CC calculations. Various evidences have also

*[*]rprajapat@ph.iitr.ac.in
[†]Corresponding author: moumita.maiti@ph.iitr.ac.in

been found that manifested the strong influence of positive Q-value neutron transfer (PQNT) in sub-barrier fusion cross-section enhancements [14,18–22]. Likewise, in ^{40}Ca + ^{70}Zn [12], ^{40}Ca + ^{124}Sn [18], ^{60}Ni + ^{100}Mo [19], ^{40}Ca + ^{194}Pt, ^{192}Os [21], ^{124,132}Sn + ^{40,48}Ca [22], and ^{28}Si + ^{94}Zr [14] systems, the enhanced sub-barrier fusion cross section was witnessed due to PQNT channels. This is due to the gain in energy at some intermediate states caused by PQNT substantially increased the sub-barrier fusion probability [23]. However, many systems, for instance, ^{32}S + ^{112,116}Sn [8], ^{132}Sn + ^{58}Ni [24], ^{18}O + ^{74}Ge [25] have been reported recently which do not show any additional enhancement of cross sections in sub-barrier fusion despite having PQNT channels. Whereas in some of such cases, the inclusion of couplings to collective states was only able to explain the sub-barrier fusion enhancement. In a systematic study, it has also been pointed out that enhancement in the sub-barrier fusion cross section due to the PQNT channel should be revised as it is observed only if the deformation of colliding nuclei increases significantly after neutron transfer [26].

The influence of couplings with the relative motion split the one-dimensional barrier into a continuous barrier distribution (BD) which provides the necessary fingerprint of nuclear structure of colliding nuclei [7]. Extraction of the BD is twofold: (i) precise fusion measurements and (ii) quasielastic (QE) scattering. The fusion BD could be extracted from the fusion cross section σ_{fus} with respect to the center-of-mass energy $E_{\text{c.m.}}$ by taking the double derivative of the product $\sigma_{\text{fus}} E_{\text{c.m.}}$, $d^2(\sigma_{\text{fus}} E_{\text{c.m.}})/dE_{\text{c.m.}}^2$, whereas QE scattering at back-angle (θ) is the sum of all processes excluding capture (fusion). It consists of elastic, inelastic, and transfer channels whose BD can be obtained from the first derivative of the ratio of differential quasielastic ($d\sigma_{\text{QE}}$) and Rutherford cross sections ($d\sigma_R$) at a given energy ($E_{\text{c.m.}}$) [27],

$$D_{\text{QE}}(E_{\text{c.m.}}, \theta) = -\frac{d}{dE_{\text{c.m.}}} \left[\frac{d\sigma_{\text{QE}}}{d\sigma_R} (E_{\text{c.m.}}, \theta) \right]. \quad (1)$$

Both approaches (fusion and QE scattering) usually give a similar shape of the BD as examined only in a few studies [27–29]. Up to now, a few attempts have been made to determine the higher-order hexadecapole deformation (β_4) experimentally using the QE barrier distribution as a probe in ^{16}O + ^{152}Sm, ^{170}Er, ^{174}Yb [30], and ^{24}Mg + ^{90}Zr systems [31]. It may help to benchmark the macroscopic-microscopic theories, which is imperative for exploiting the nuclear chart. Moreover, back-angle QE barrier distributions have extended their reach towards the cold and hot fusion reactions to decide the optimum incident energy for the production of super-heavy elements [32,33]. It again reinvigorates the interest in this research area. Besides, processes, such as precompound emission [34,35], complete, and incomplete fusion (particularly for ^{6}Li and ^{7}Li projectiles) [36–40], and fusion-fission [41,42] have also been found to emerge at energies $\leqslant$10 MeV/nucleon.

It is understood from the literature that the influence of couplings on the PQNT transfer channels in the sub-barrier fusion is ambiguous and an enduring open question due to the scarcity of comprehensive data sets. Also, the impact of couplings on collective states of interacting nuclei on BDs

(from fusion and QE scattering) is quite dramatic and must be explored. In light of this, the present investigation aims to examine the role of the PQNT effect in sub-barrier fusion and to check whether the shape of barrier distributions from fusion and QE scattering (D_{fus} and D_{QE}) are the same. Thus, excitation functions of fusion and QE scattering at back-angles ($\theta_{\text{lab}} = 138°, 150°$) have been measured for the ^{30}Si + ^{156}Gd reaction at energies $\approx$13% below to $\approx$9% above the Coulomb barrier.

The article is organized as follows; Sec. II presents the experimental method; results and interpretation of data are discussed in Sec. III. Finally, Sec. IV concludes the paper.

II. EXPERIMENTAL METHOD

The experiment was performed at the 15 UD Pelletron accelerator facility of Inter-University Accelerator Center (IUAC), New Delhi, India. A pulsed beam of ^{30}Si with 2- and 4-μs pulse separations at above and below Coulomb-barrier energies, respectively, was bombarded on a thin ^{156}Gd target. Isotopically enriched (95.4%) thin ^{156}Gd target foils, thickness of $\approx$100.7 μg/cm^2, fabricated on $\approx$30-μg/cm^2-thick carbon backing, faced the beam during the experiment. The fabrication, purity, and thickness check of ^{156}Gd targets using various characterizations (viz. Rutherford back scattering, Energy dispersive x-ray spectroscopy, etc.) has been performed at the IUAC [43]. Beam energy (E_{lab}) was varied between 108 and 136 MeV covering $\approx$13% below to $\approx$9% above the Coulomb barrier. The Bass barrier of the ^{30}Si + ^{156}Gd system is 105.1 MeV in the center-of-mass frame (125.3-MeV laboratory equivalent). The beam energy loss across the carbon thickness and at the half-thickness of the ^{156}Gd target was calculated using the SRIM software [44], and corrected energy was used for analysis. The Heavy Ion Reaction Analyser (HIRA) [45] facility was used for our measurements. HIRA rejects primary beamlike particles with respect to the beam direction and transports recoiling evaporation residues (ERs) from the target chamber to the focal plane, dispersing them according to their m/q ratio. It was operated at $\theta_{\text{lab}} = 0°$ with regard to the beam direction with solid angle acceptance of 5 mSr (2.2° polar angle).

In the target chamber, two solid-state silicon detectors (SSSDs), each with a circular aperture of 1-mm diameter, were placed on the horizontal plane at $\theta_{\text{lab}} = 15.5°$ to monitor the beam and absolute normalization of ER cross-sectional data. Also, to detect the backscattered QE events (including elastic, inelastic, and neutron transfer, which are indistinguishable), two SSSDs were installed in a sliding seal target chamber at two different back-angles $\theta_{\text{lab}} = 138°$ and $150°$, having opening apertures of 2 and 4 mm, respectively. The typical view of the target chamber is shown in Fig. 1. A carbon foil of thickness $\approx$10 μg/cm^2 was placed 10 cm downstream from the target to reset the charge state of ERs to the equilibrium distribution.

To detect the recoiling heavy ERs, a multiwire proportional counter (MWPC), having dimensions of 15×5 cm^2 in the XY direction, was placed at the focal plane of HIRA. The isobutane gas pressure in MWPC was maintained at 5 Torr. The MWPC gives position signals (X_L, X_R, Y_U, and Y_D),
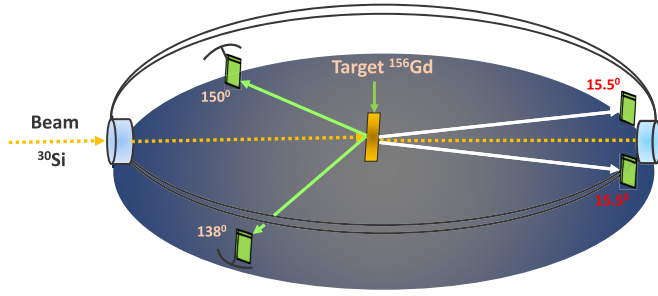
FIG. 1. A schematic of the target chamber used in the present experiment.

energy loss (ΔE), and the timing signal. The master strobe was generated by obtaining a logical OR between time signals from two monitor detectors, two QE back detectors, and the MWPC anode signal for the data-acquisition system. The time of flight (TOF) was obtained using the time to amplitude converter by considering the MWPC anode signal as the start signal and a suitably delayed radio-frequency (rf) pulse as the stop signal.

Whereas setting the apparatus, the spectrometer field was scanned to find the most probable charge state, mass, and energy of ERs for the $^{30}\text{Si} + ^{156}\text{Gd}$ reaction at $E_{\text{lab}} = 127.4$ MeV. The best setting was obtained by looking for maximum transmission efficiency and clear separation of ERs from the beamlike particles at each incident energy. As one can see, in the two-dimensional spectra of ER energy loss
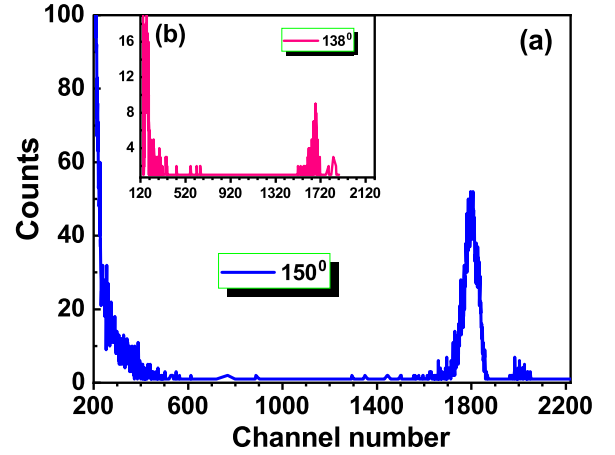

FIG. 3. Measured spectra of QE events recorded using solid-state silicon detectors at back-angles (a) $\theta_{\text{lab}} = 150°$ and (b) $\theta_{\text{lab}} = 138°$.

(ΔE) vs ER TOF at $E_{\text{c.m.}} = 113.6$, 103.5, and 91.7 MeV presented in Figs. 2(a)–(c), respectively, the ERs are well separated from beamlike particles. At lowest-energy $E_{\text{c.m.}} = 91.7$ MeV, at $\approx 13\%$ below the Coulomb barrier, a blank run was recorded for a few hours with no target in which hardly a few events were registered within the ER-gated region, shown in Fig. 2(d).

Figures 3(a) and 3(b) show a typical two-dimensional correlation plot of measured QE data (channel number vs counts).
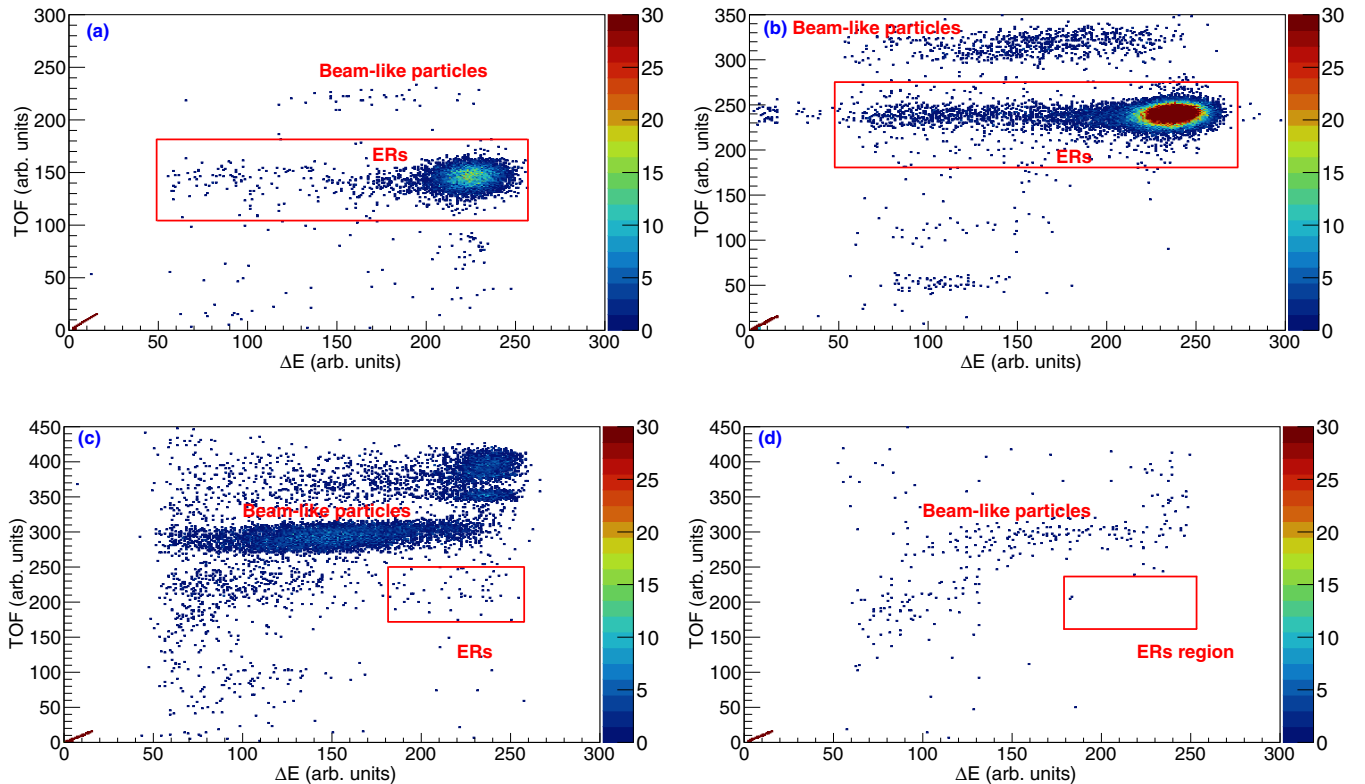

FIG. 2. Scatter plots between ER energy loss (ΔE) and ER TOF for the $^{30}\text{Si} + ^{156}\text{Gd}$ fusion reaction at (a) $E_{\text{c.m.}} = 113.6$ MeV, (b) $E_{\text{c.m.}} = 103.5$ MeV, (c) $E_{\text{c.m.}} = 91.7$ MeV, and (d) $E_{\text{c.m.}} = 91.7$ MeV with no target. The red contours represent the group of ERs which are well separated from beamlike particles.
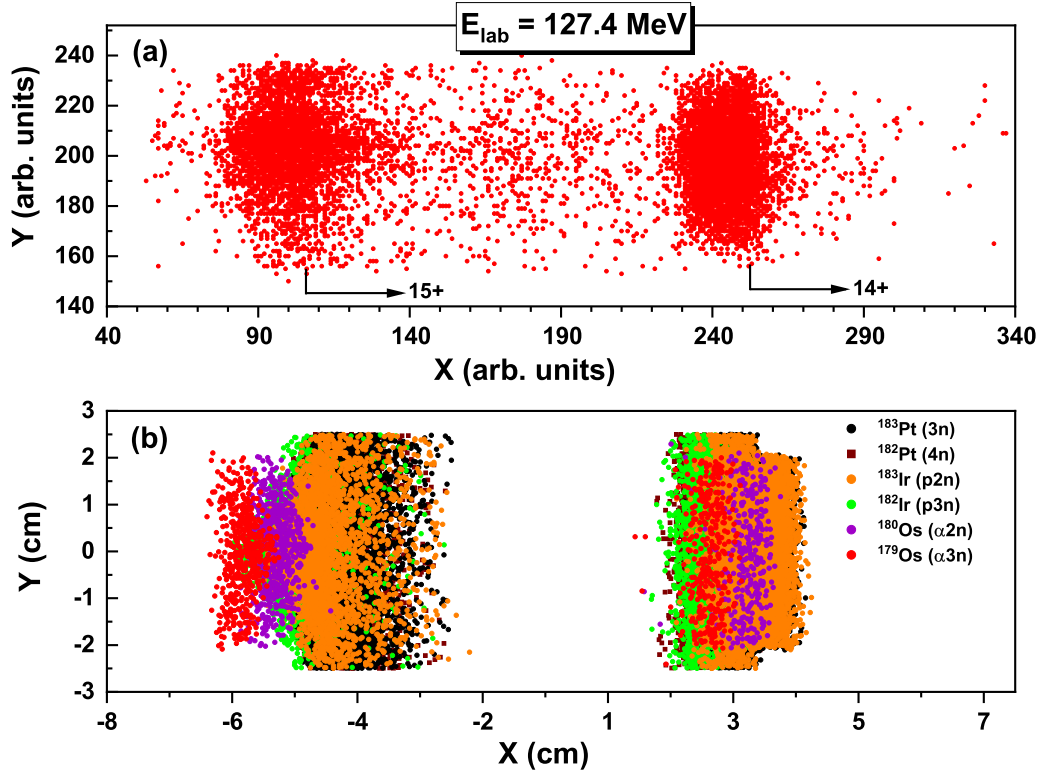
FIG. 4. Two-dimensional MWPC X-Y position spectrum obtained from (a) experiment, and (b) simulation using the TERS code [48] for the ^{30}Si + ^{156}Gd reaction at $E_{\text{lab}} = 127.4$ MeV.

Here, the area under the main peak includes indistinguishable elastic, inelastic, and transfer events. The data between channel numbers $\approx$1200-1920 and $\approx$1200-1750 for $\theta_{\text{lab}} = 150°$ and $\theta_{\text{lab}} = 138°$, respectively, are considered as QE (Fig. 3). Following the two-body kinematics, special attention has been paid during the offline analysis to avoid any contaminating channels which may arise from the higher mass impurities of the target (enrichment 95.4%). Off-beam data analysis work has been carried out using the CANDLE software [46].

III. RESULTS AND DISCUSSION

A. Analysis of fusion cross section

The measured total ER cross section has been considered as the fusion cross section for the ^{30}Si + ^{156}Gd system as the predicted fusion-fission cross section from the statistical model code PACE4 [47] is negligible within the studied energy range. The fusion cross sections of ^{30}Si + ^{156}Gd have been estimated following the procedure described in Ref. [9] with the help of measured ERs, yield of monitor detectors, and average transmission efficiency of HIRA. The semimicroscopic Monte Carlo code TERS [48] estimates the average transmission efficiency of HIRA with $\approx$10% uncertainty, whereas it was found to be 8.2% at $E_{\text{lab}} = 135.4$ MeV for the ^{30}Si + ^{156}Gd system. The simulation has been performed for 3×10^5 Monte Carlo events for each configuration. One such simulated spectrum of various dominant ERs was generated along with the experimental spectrum between the X and Y positions of MWPC gated by ERs of the ΔE-TOF spectrum

at $E_{\text{lab}} = 127.4$ MeV, shown in Fig. 4. One can see that the experimentally obtained two-dimensional X-Y position spectrum of ERs is in good agreement with the simulated one. A more detailed procedure for estimating the transmission efficiency of HIRA using the TERS code can be found in Ref. [49]. The measured fusion cross section has been presented in Table I. The associated uncertainty in the cross-section measurement is considered from the: (i) statistical

TABLE I. Measured fusion cross section (σ_{fus}) from the ^{30}Si + ^{156}Gd reaction at various energies ($E_{\text{c.m.}}$) and the associated uncertainties $\delta\sigma_{\text{fus}}$.

Energy ($E_{\text{c.m.}}$) (MeV)	σ_{fus} (mb)	$\pm\delta\sigma_{\text{fus}}$ (mb)
91.7	0.017	0.003
93.4	0.12	0.02
95.1	1.04	0.14
96.8	3.6	0.5
98.4	8.9	1.2
100.1	18.1	2.4
101.8	38.4	5.0
103.5	57.1	7.4
105.2	96.3	12.5
106.8	124.4	16.2
108.5	168.8	22.0
110.2	200.9	26.3
111.9	245.7	32.3
113.6	279.5	36.8

TABLE II. Excited states (λ^π) with excitation energies (E^*) and corresponding deformation parameters (β_λ) [53,54] of ^{30}Si and ^{156}Gd used in the coupled-channel calculations.

Nucleus	E^* (MeV)	λ^π	β_λ
^{30}Si	2.235	2^+	-0.236
	5.487	3^-	0.275
^{156}Gd	0.089	2^+	0.26
	0.2882	4^+	0.089

error in ER counts and monitor yields and (ii) uncertainty in determining HIRA's transmission efficiency.

CC calculations have been performed using CCFULL [50] to interpret the measured data. It predicts the total fusion cross section and average angular momenta by considering various inelastic channel couplings in the interacting nuclei. Use of various ion-ion nuclear potentials, such as proximity (prox) 77, prox 88, prox 2000, Bass 80, etc. [51,52], are seen in the literature to explain heavy-ion fusion dynamics. However, Woods-Saxon ion-ion potential with Akyüz-Winther (AW) parametrization is used in the present analysis with well depth (V_0) = 80.0 MeV, radius parameter (r_0) = 1.16 fm,

and diffuseness (a) = 0.74 fm. These potential parameters have been adjusted to obtain a good fit to data in the above-barrier region and to reproduce equivalent Coulomb barrier parameters, barrier height (V_b) = 104.43 MeV, barrier radius (r_b) = 11.47 fm, and curvature = 3.82 MeV. The nuclear structural information of ^{30}Si and ^{156}Gd on the low-lying collective modes are listed in Table II.

The measured fusion excitation function is compared with 1D-BPM (without any coupling) in Fig. 5(a). Furthermore, CC calculations have been employed to understand the influence of coupling of the vibrational states of the ^{30}Si projectile (p) and rotational states of the ^{156}Gd target (t) along with the $2n$-transfer channel on the fusion excitation function (EF), and its subsequent barrier distribution, shown in Figs. 5 and 6. It can be observed from Fig. 5(b) that the sub-barrier fusion cross section predicted by 1D-BPM is significantly lower than the measured data. Therefore, the projectile's (^{30}Si) excitation of the 2^+ state with one-phonon (1ph) and ^{156}Gd as inert were considered in the CCFULL that enhances cross sections as compared to 1D-BPM in the sub-barrier domain, yet it still underpredicts the data. Hence, coupling of various rotational excited states of the target denoted by "NRot" [the number of levels in the rotational band along with ground state (g.s.)] (NRot=1–4) and projectile as inert were considered one by
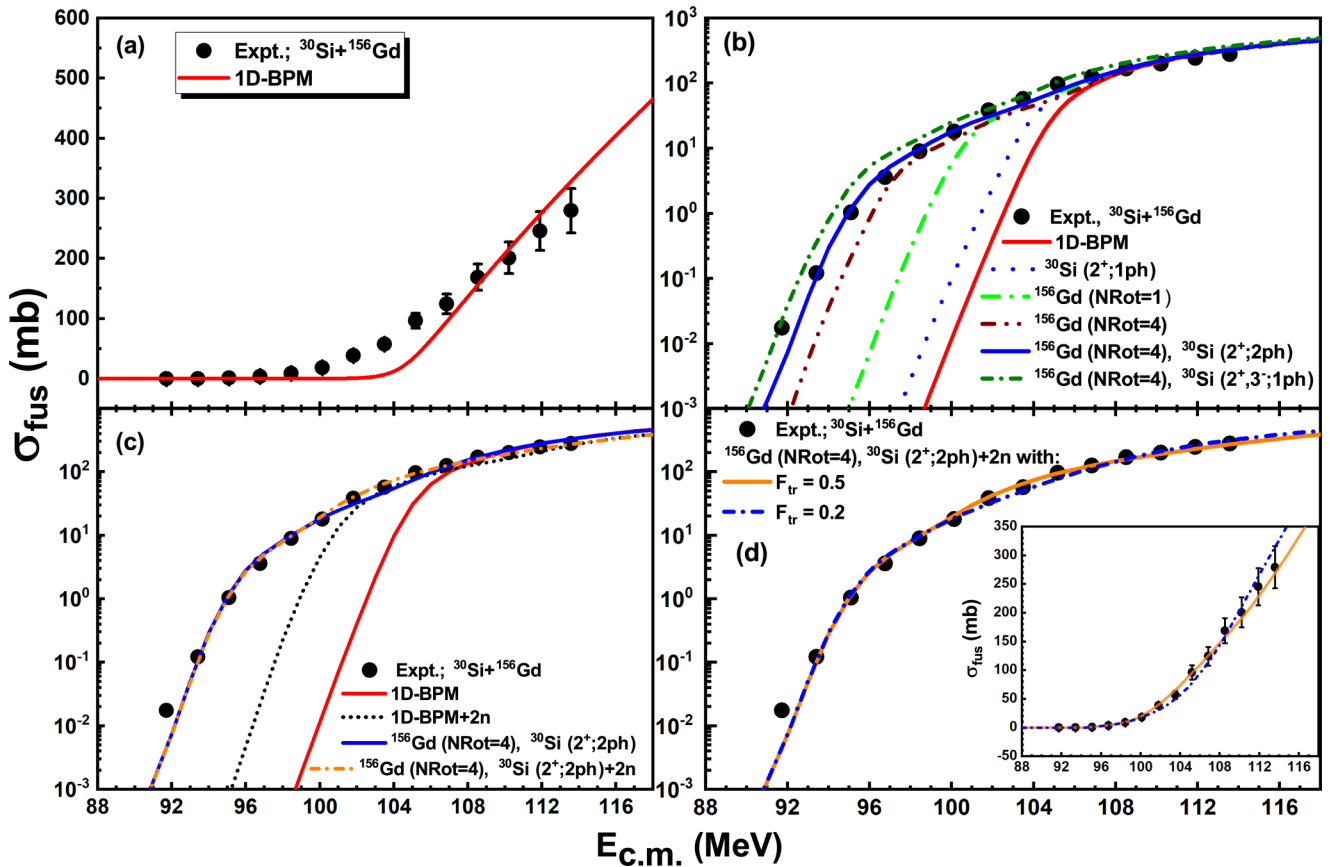

FIG. 5. (a) Experimental fusion excitation function of the ^{30}Si + ^{156}Gd reaction is compared with (a) 1D-BPM (solid red line), (b) considering different modes of collective excitations in projectile and target, (c) coupling of the $2n$-transfer channel along with inelastic excitations between the interacting partners, and (d) $2n$-transfer channel coupling besides inelastic excitations in interacting nuclei with two different transfer coupling strength parameter (F_{tr}), using the CCFULL code (see the text for details).
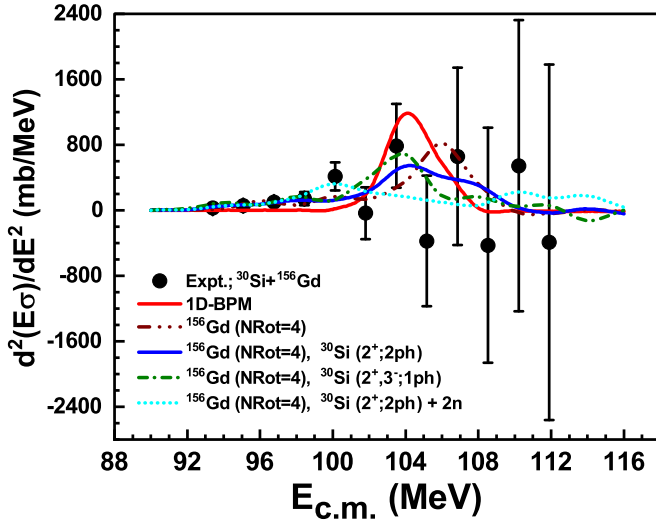
FIG. 6. The experimental fusion barrier distributions (D_{fus}) for the $^{30}\text{Si} + ^{156}\text{Gd}$ system compared with the theoretical predictions from CCFULL.

one; depicted only NRot=1 and 4 in Fig. 5(b) to avoid the crowd. For instance, if NRot=1, the 2^+ state of the target is included with the ground-state (0^+). Furthermore, coupling of rotational states NRot=4 ($0^+, 2^+, 4^+, 6^+,$ and 8^+) of the target significantly enhanced the sub-barrier fusion cross section as compared to NRot=1 but failed to reproduce the measured data. It is worth mentioning here that the inclusion of more rotational states of the target, such as NRot=5 ($0^+, 2^+, 4^+, 6^+,$ $8^+,$ and 10^+), does not further enhance the sub-barrier fusion cross section. The couplings to the rotational band of the target up to NRot=4 are more robust than the coupling of the projectile's vibrational states. However, individual coupling of the projectile and the target cannot reproduce the cross-section data at below barrier energies. Thus, the combined effect of *p-t* and mutual excitations of *p* states were incorporated into the calculations. The consideration of two-phonon (2ph) 2^+ state of ^{30}Si and target's rotational states up to 8^+ (NRot=4) further enhances the magnitude of the sub-barrier fusion cross sections, and the combination of collective excitations in *p-t* successfully explained the experimental data throughout the energy range except at $E_{\text{c.m.}} = 91.7$ MeV. Since ^{30}Si has a sizable negative quadrupole moment ($\beta_2 = -0.236$) with smaller excitation energy of 2^+ (2.235-MeV) state, its effect is significantly visible in the calculations. Inclusion of rotational states up to 8^+ (NRot=4) in target and one-phonon 2^+ and 3^- states in the projectile with mutual excitations, i.e., $2^+ \otimes 3^-$, in the CC calculation reproduces the one lowest-energy point and data above $E_{\text{c.m.}} = 100$ MeV but overestimates them between $E_{\text{c.m.}} = 92$–100 MeV. A large part of this overestimation in predicted cross sections might be due to large octupole deformation of the projectile and mutual excitations between $2^+, 3^-$ states of ^{30}Si. However, it is essential to emphasize that $E_{\text{c.m.}} = 91.7$ MeV is the limit in the current measurement as the background starts contaminating the actual events at this energy and below.

The CCFULL calculations were also performed by considering ^{30}Si as a rotor and ^{156}Gd as a vibrator. CC calculations

were performed with various rotational states of ^{30}Si by considering NRot=1–4 and $2^+, 3^-$ vibrational states of ^{156}Gd with 1 and 2 phonons one after the other. It has been noted that projectiles' rotational state coupling is insignificant after NRot=2. Even after considering the inelastic excitations of projectiles' rotational states (NRot=2) and mutual excitations in $2^+, 3^-$ vibrational states of the target with two-two phonons in each were not able to reproduce data well.

The present system ($^{30}\text{Si} + ^{156}\text{Gd}$) has one positive Q value of $+0.8$ MeV for 2n pickup (by the projectile from the target), and all other pickups and stripping transfer channels have negative Q values as listed in Table III. Thus, the 2n transfer should be more localized, and the formation of a 2n pair (boson) would enhance the transfer probability. Thus, CCFULL calculations have been performed with 2n-transfer channel couplings along with collective excitations in participating nuclei to examine the effect of PQNT on sub-barrier fusion as depicted in Figs. 5(c) and 5(d). CCFULL allows pair transfer couplings between the ground states of interacting nuclei through the macroscopic transfer coupling form factor as given in Ref. [55],

$$F_{\text{transfer}}(r) = F_{\text{tr}}\frac{dV_N}{dr}, \qquad (2)$$

where F_{tr} and V_N are the coupling strength parameter and attractive nuclear potential, respectively. Although 2n-transfer coupling with $F_{\text{tr}} = 0.5$ along with 1D-BPM in CCFULL calculations enhanced the sub-barrier fusion cross sections relative to 1D-BPM but could not reproduce the experimental data. Hence, 2n-transfer channel (with $F_{\text{tr}} = 0.5$) along with collective excitations of fusing nuclei was considered as shown in Fig. 5(c). Since the combination of ^{156}Gd (NRot=4), ^{30}Si ($2^+; 2\text{ph}$) channels grossly explains the measured data except for $E_{\text{c.m.}} = 91.7$ MeV, hence, this combination has been chosen for the inclusion of 2n-transfer channel coupling. It is visible here that the inclusion of 2n-transfer channel couplings improved the explanation of measured data around the Coulomb barrier ($E_{\text{c.m.}} = 98$–106 MeV). However, those predictions do not anticipate any significant fusion cross-section enhancement at below barrier energy (< 100 MeV). Furthermore, coupling strength (F_{tr}), which is a phenomenological parameter, is tested to fit the experimental data as performed in Refs. [13,14] also. Thus, CCFULL calculations were performed with 2n-transfer channel couplings for coupling strength parameters, $F_{\text{tr}} = 0.2$-0.5, along with collective excitations in the projectile and target as presented in Fig. 5(d). For clear visualization of the influence of F_{tr} around and above barrier energies, the figure is shown in a linear scale at the inset of Fig. 5(d). One can note that as the F_{tr} value increases, the fusion cross section gets reduced at energies near to above the Coulomb barrier, whereas no significant effect has been observed at sub-barrier energy points. Nevertheless, coupling strength parameter $F_{\text{tr}} = 0.5$ MeV provides the best fit for experimental data near the Coulomb barrier and beyond.

However, it is to be noted that role of the 2n-transfer channel is uncertain in the present paper as the inelastic couplings themselves overestimate [see Fig. 5(b)] the measured sub-barrier fusion cross section.

TABLE III. $Q_{+xn(-xn)}$ (MeV) values for multineutron pickup (by projectile from target) and stripping transfer channels from g.s. to g.s. of interacting nuclei for the ^{30}Si $+$ ^{156}Gd system.

Reaction	$Q_{+1n(-1n)}$	$Q_{+2n(-2n)}$	$Q_{+3n(-3n)}$	$Q_{+4n(-4n)}$	$Q_{+5n(-5n)}$	$Q_{+6n(-6n)}$
^{30}Si $+$ ^{156}Gd	-1.9 (-4.2)	$+0.8$ (-4.8)	-3.6 (-16.0)	-2.3 (-21.9)	-8.4 (-35.3)	-8.8 (-43.4)

B. Fusion barrier distribution

The barrier distribution in heavy-ion collisions demonstrates the wealth of explicit information concerning the nuclear structure effects of the colliding nuclei. It has been recognized that couplings between their relative motion and other nuclear degrees of freedom, such as static deformation, nucleon transfer, etc., split the single fusion barrier into a distribution of barriers which is a major factor of sub-barrier fusion enhancement relative to 1D-BPM. Thus, BD can be extracted from the measured fusion cross-section (σ_{fus}), taking a double derivative of the energy-weighted σ_{fus} with respect to energy [Eq. (3)],

$$D_{\text{fus}} = \frac{d^2(E\sigma_{\text{fus}})}{dE^2}. \quad (3)$$

The double derivative of $E\sigma_{\text{fus}}$ (fusion BD) and associated uncertainty has been calculated using the three-point-difference formula prescribed in Ref. [7]. The uncertainty of BD increases with the increase in absolute error in σ_{fus} and growing energy; hence, poorly defined at higher energies. In Fig. 6, the experimental fusion BD is compared with the theoretical calculations based on the inclusion and exclusion of couplings in the *p-t* nuclei.

The BD from the theoretical cross sections was extracted in the energy step of $\Delta E = 2$ MeV to obtain a smooth curve [7]. The calculated BD from 1D-BPM has a single peak around the Coulomb barrier, and it could not explain the experimental BD (Fig. 6). An improvement in the shape of BD was observed by considering the theoretical calculations with rotational couplings in target NRot=4 (0^+, 2^+, 4^+, 6^+, and 8^+ states) and 2ph 2^+ vibrational state excitation in the projectile, which also reasonably explained the fusion data (Fig. 5), and it could explain the experimental BD except for the peak around 100 MeV. The ^{30}Si $+$ ^{156}Gd system has a positive Q value for 2n transfer, and fusion data were improved around 100 MeV after incorporating the transfer channel coupling. Thus, theoretical BD was obtained with the same inelastic couplings with 2n-transfer channel ($F_{\text{tr}} = 0.5$), which implies that the barrier peak was shifted towards the lower-energy side and matched with the low-energy experimental data around 100 MeV which may be due to the 2n-transfer effect. However, this theoretical combination could not reproduce the experimental BD around the Coulomb barrier and is broad.

C. ECC model

It has been observed from CCFULL predictions that transfer channel coupling does not produce a significant effect on the sub-barrier fusion cross sections despite having a positive Q value for two-neutron pickup ($Q_{2n} = +0.8$ MeV) channel in the present system. Thus, the ECC model [17] has been employed, which considers the inelastic as well as multineu-

tron transfer channels to estimate the fusion cross section. The ECC model is based on the semiclassical approach where the quantum penetration probability of the Coulomb barrier is calculated using the hypothesis of barrier distribution appearing due to the multidimensional feature of the real nucleus-nucleus interaction. This model incorporates the multineutron transfer channels, thus, incoming flux may penetrate the multidimensional Coulomb barrier in the different neutron transfer channels.

All the calculations in this model have been performed using Woods-Saxon potential with AW parameters $V_0 = 80.0$ MeV, $r_0 = 1.166$, and $a = 0.76$ fm. The coupling parameters, vibrational excitations in projectile and rotational excitation in target, are taken from Table II. The stiffness parameters (C) required for the ECC calculations were used from the liquid-drop model [17].

ECC calculations were performed with: (i) 1D-BPM (without coupling), presented by the solid red line in Fig. 7, and (ii) low-lying quadrupole ($\lambda = 2$) and octupole ($\lambda = 3$) vibrations in ^{30}Si one after other and rotational coupling in ^{156}Gd by considering with and without the transfer ($2n$) channel as shown in Fig. 7. ECC predictions with collective excitations in the projectile (quadrupole vibrations) and target without the transfer channel agree with the experimental data throughout the energy range except for two lowermost energy points.
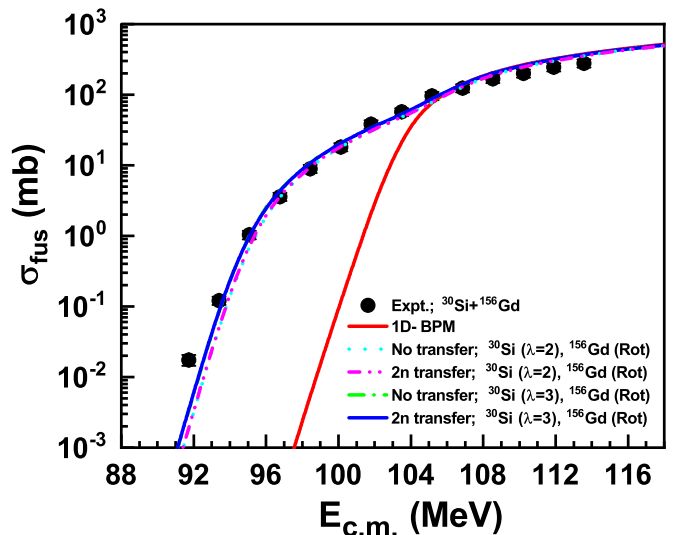

FIG. 7. The experimental fusion excitation function of ^{30}Si $+$ ^{156}Gd compared with theoretical predictions considering with and without neutron transfer channel along with vibrational excitations (quadrupole and octupole) in the projectile one after other and rotational (Rot) one in target during the ECC model (see the text for details). It may be noted that curves with transfer and no-transfer overlap with each other.

Hence, two neutron transfer channels with positive Q values ($Q_{2n} = +0.8$ MeV) with the collective excitations in *p-t* nuclei were included in the calculation. However, no effect of the $2n$ transfer channel has been observed in fusion cross sections. Coupling to the projectile's low-lying octupole ($\lambda = 3$) vibrations with the target's rotational couplings was incorporated in ECC calculations, excluding the $2n$-transfer channel and by taking into account the $2n$-transfer channel. The inclusion of octupole vibrational couplings in the projectile slightly enhances the sub-barrier fusion cross section compared to quadrupole vibrational couplings. One can see that the ECC calculations with and without neutron transfer into account give satisfactory agreement with the experimental data over the entire energy range except for $E_{\text{c.m.}} = 91.7$ MeV. Predictions of the ECC model (with and without the neutron transfer channel) are overlapping throughout the energy range, which implies that present data do not show any significant effect of the positive Q value of $2n$ transfer in the ^{30}Si + ^{156}Gd reaction. However, the uncertainties observed between CCFULL and ECC predictions for transfer reaction might be due to the different approaches adopted by the model codes, quantum-mechanical coupled channel by CCFULL, and semiclassical empirical coupling channel approach in the ECC model. Thus, it is not easy to conclude the role of the $2n$-pickup transfer in the present paper.

D. QE excitation function and BD

With the help of area counts under the central peak (Fig. 3) and Eq. (4), the ratio between differential quasielastic and Rutherford scattering cross sections have been extracted experimentally at given projectile energy and back angle,

$$\frac{d\sigma_{\text{QE}}}{d\sigma_R}(\theta_{\text{back}}) = \left[\frac{N_{\text{back}}(\theta_{\text{back}})}{N_{\text{mon}}(\theta_{\text{mon}})}\right]\left[\frac{d\sigma_R/d\Omega(\theta_{\text{mon}})}{d\sigma_R/d\Omega(\theta_{\text{back}})}\right]\left[\frac{\Delta\Omega_{\text{mon}}}{\Delta\Omega_{\text{back}}}\right],$$
(4)

with

$$\left[\frac{\Delta\Omega_{\text{mon}}}{\Delta\Omega_{\text{back}}}\right] = \left[\frac{N_{\text{mon}}^{Gd}(\theta_{\text{mon}})}{N_{\text{back}}^{Gd}(\theta_{\text{back}})}\right]\left[\frac{d\sigma_R^{Gd}/d\Omega(\theta_{\text{back}})}{d\sigma_R^{Gd}/d\Omega(\theta_{\text{mon}})}\right], \quad (5)$$

where $N_{\text{back}}(\theta_{\text{back}})$ and $N_{\text{mon}}(\theta_{\text{mon}}) = \sqrt{M_L M_R}$ are the number of events registered in the back detector (at angle θ_{back}) and left-right monitor detectors (at angle θ_{mon}), respectively; while $\Delta\Omega_{\text{back}}$ and $\Delta\Omega_{\text{mon}}$ represent the corresponding solid angles whose ratio is calculated [using Eq. (5)] at the lowest-energy point to ensure dominance of Rutherford scattering and no open transfer channel. The measured excitation functions of the differential QE scattering cross section relative to the Rutherford cross section ($d\sigma_{\text{QE}}/d\sigma_R$) at two back angles are shown in Fig. 8, which are in close proximity.

The measured values of $d\sigma_{\text{QE}}/d\sigma_R$ range between 0.08–1.0 and 0.2–1.0 for 150° and 138°, respectively, within the studied energy range. The uncertainties in the measured EFs account for statistical and systematic errors. On the higher-energy side, the associated error in QE EFs is more than the low-energy points because of low statistics.

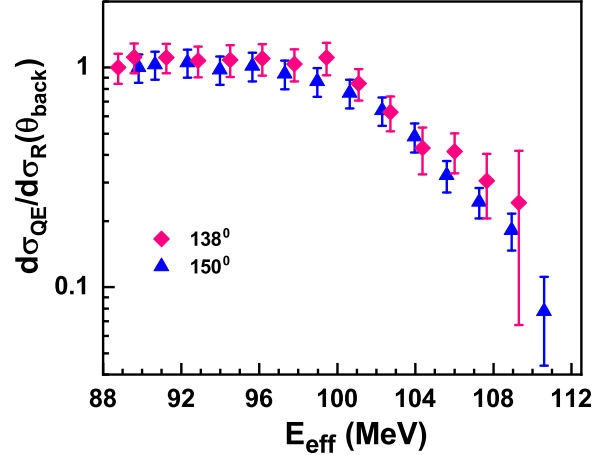Since QE events rely on the detection angle, the backscattered QE events at 150° and 138° Laboratory angles are

FIG. 8. Quasielastic scattering excitation function plot for the ^{30}Si + ^{156}Gd system measured at two back-angles 138° and 150°.

mapped to 180° by incorporating the centrifugal energy correction and effective energy (E_{eff}) [27,56], which can be written as

$$E_{\text{eff}} = E_{\text{c.m.}} - E_{\text{c.m.}}\frac{\csc(\theta_{\text{c.m.}}/2) - 1}{\csc(\theta_{\text{c.m.}}/2) + 1}$$

$$= \frac{2E_{\text{c.m.}}}{\csc(\theta_{\text{c.m.}}/2) + 1}, \quad (6)$$

where $E_{\text{c.m.}}$ and $\theta_{\text{c.m.}}$ are the energy and the scattering angle in the center-of-mass frame, respectively.

The CC calculations are employed at distinct angles using the CCFULL code to interpret the measured data of QE scattering and their BDs at two back angles as indicated in Figs. 9 and 10. The QE barrier distribution (D_{QE}) was obtained by employing the centered difference formula to three points around each center point, for instance, if there are three effective energy points $E_{\text{eff}}^{(0)}$, $E_{\text{eff}}^{(1)}$, and $E_{\text{eff}}^{(2)}$ with corresponding ratios are $d\sigma_{\text{QE}}^{(0)}/d\sigma_R$, $d\sigma_{\text{QE}}^{(1)}/d\sigma_R$, and $d\sigma_{\text{QE}}^{(2)}/d\sigma_R$ then the BD at energy $E_{\text{eff}}^{(1)}$ is as follows:

$$D_{\text{QE}}(E_{\text{eff}}^{(1)}) = \frac{d\sigma_{\text{QE}}^{(2)}/d\sigma_R - d\sigma_{\text{QE}}^{(0)}/d\sigma_R}{E_{\text{eff}}^{(2)} - E_{\text{eff}}^{(0)}}, \quad (7)$$

with the associated uncertainty $\delta D_{\text{QE}}(E_{\text{eff}}^{(1)})$ as

$$\delta D_{\text{QE}}(E_{\text{eff}}^{(1)}) = \frac{\sqrt{\delta(d\sigma_{\text{QE}}^{(2)}/d\sigma_R)^2 + \delta(d\sigma_{\text{QE}}^{(0)}/d\sigma_R)^2}}{E_{\text{eff}}^{(2)} - E_{\text{eff}}^{(0)}}. \quad (8)$$

The CCFULL program has a separate version for quasielastic scattering that uses parameters of the real and imaginary parts of the interaction potential. For the real part, Woods-Saxon potential with the same AW parameters as used to explain the fusion cross section (Sec. III A), has been adopted for QE scattering predictions. Whereas, the potential parameters of imaginary part are as follows: depth (V_w) = 30 MeV, radius (r_w) = 1.0 fm, and diffuseness (a_w) = 0.1 fm. The choice of these parameters keeps the imaginary potential well inside the Coulomb barrier with a little strength in the surface region. If the imaginary potential is well localized inside the Coulomb
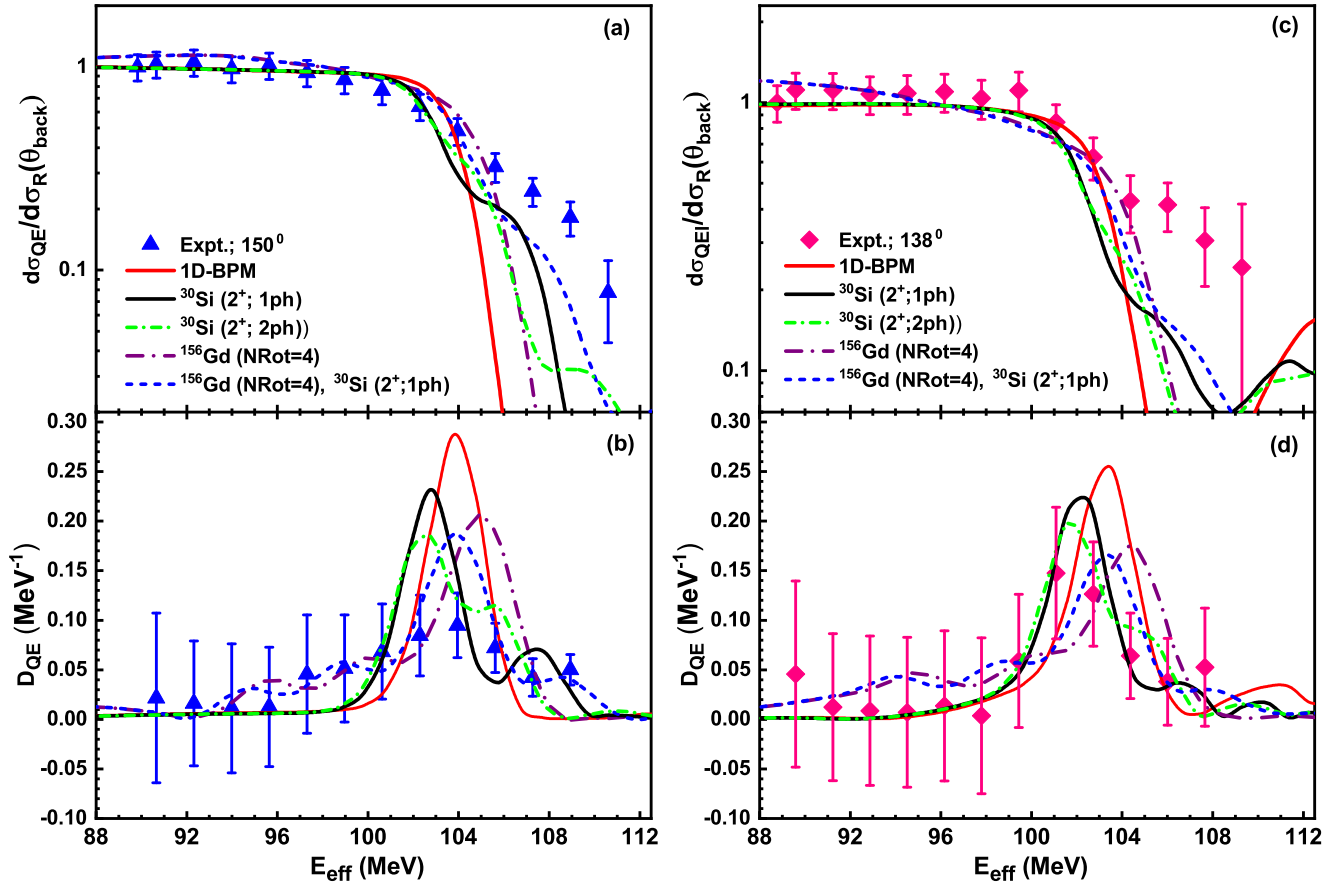
FIG. 9. Comparison between measured data from the ^{30}Si + ^{156}Gd reaction for the QE excitation function and CC calculations with different inelastic coupling options using CCFULL at (a) $\theta_{lab} = 150°$, (c) $\theta_{lab} = 138°$. Panels (b) and (d) show corresponding barrier distributions.

barrier, the predictions are insensitive to parameters of the imaginary part, pointed out in Refs. [57,58].

Figures 9(a) and 9(b) represent the measured QE excitation function and BD, respectively, at back-angle $\theta_{lab} = 150°$ along with the theoretical calculations performed using various collective excitations in *p-t* as described in Sec. III A for interpretation of fusion data. The no-coupling (1D-BPM) results fail substantially to explain the QE EF and BD; similarly, incorporation of one and two phonon 2^+ state excitation of ^{30}Si does not reproduce the measured data at above barrier energy points but successfully explains it in the lower-energy zone. The effects of rotational couplings of 0^+, 2^+, 4^+, 6^+, and 8^+ (NRot=4) states of the target are found to be slightly larger than 0^+ and 2^+ (NRot=1) states but fail to intimate the experimental data around and above the Coulomb barrier domain. The centroid of BD was shifted by 1 MeV towards higher energy due to the rotational coupling of the target.

For further improvement, rotational excitations in the target (NRot=4) and one-phonon 2^+ state in projectile were adopted, which certainly improved the data fit around the Coulomb barrier, yet failed to retrace the data in the above barrier zone and a little bit overpredicted in lower-energy region. It suggests the necessity of inelastic (IE) couplings with the 2*n*-transfer channel.

Similarly, the QE excitation function at another back-angle $\theta_{lab} = 138°$ and corresponding BD are plotted with theoretical

predictions from CFULL as shown in Figs. 9(c) and 9(d). In the no-coupling limit (1D-BPM), experimental data are reproduced in the low-energy domain but fail to explain the data at higher energies. The CC calculations obtained by including couplings to the one- and two-phonon 2^+ vibrational state one after other in the projectile are insufficient to explain the high-energy QE EF but successfully demonstrate the BD. It should be noted that the peak of BD is shifted by 2 MeV towards the lower-energy side after considering the vibrational couplings in the projectile. Subsequently, even the inclusion of rotational couplings up to 8^+ states (NRot=4) in target and collective couplings between *p-t* nuclei do not add much in explaining the measured QE scattering data and subsequent BD towards a higher-energy zone.

Thus, IE couplings, along with 2*n*-transfer channel with various F_{tr} values, are employed to reproduce the QE data and its BD, shown in Fig. 10. For $\theta_{lab} = 150°$, IE couplings in ^{30}Si, along with the 2*n*-transfer channel with $F_{tr} = 0.3$ and 0.35, are employed that reproduce the QE data except at a few above barrier energy points and corresponding BD is oscillatory in nature. Furthermore, incorporation of the IE in *p-t* nuclei + 2*n*-transfer channel with coupling strength parameters $F_{tr} = 0.25$ and 0.34, results in grossly explaining the QE data throughout the energy range [Fig. 10(a)] but slightly overpredicting the measured data in the lower-energy zone.
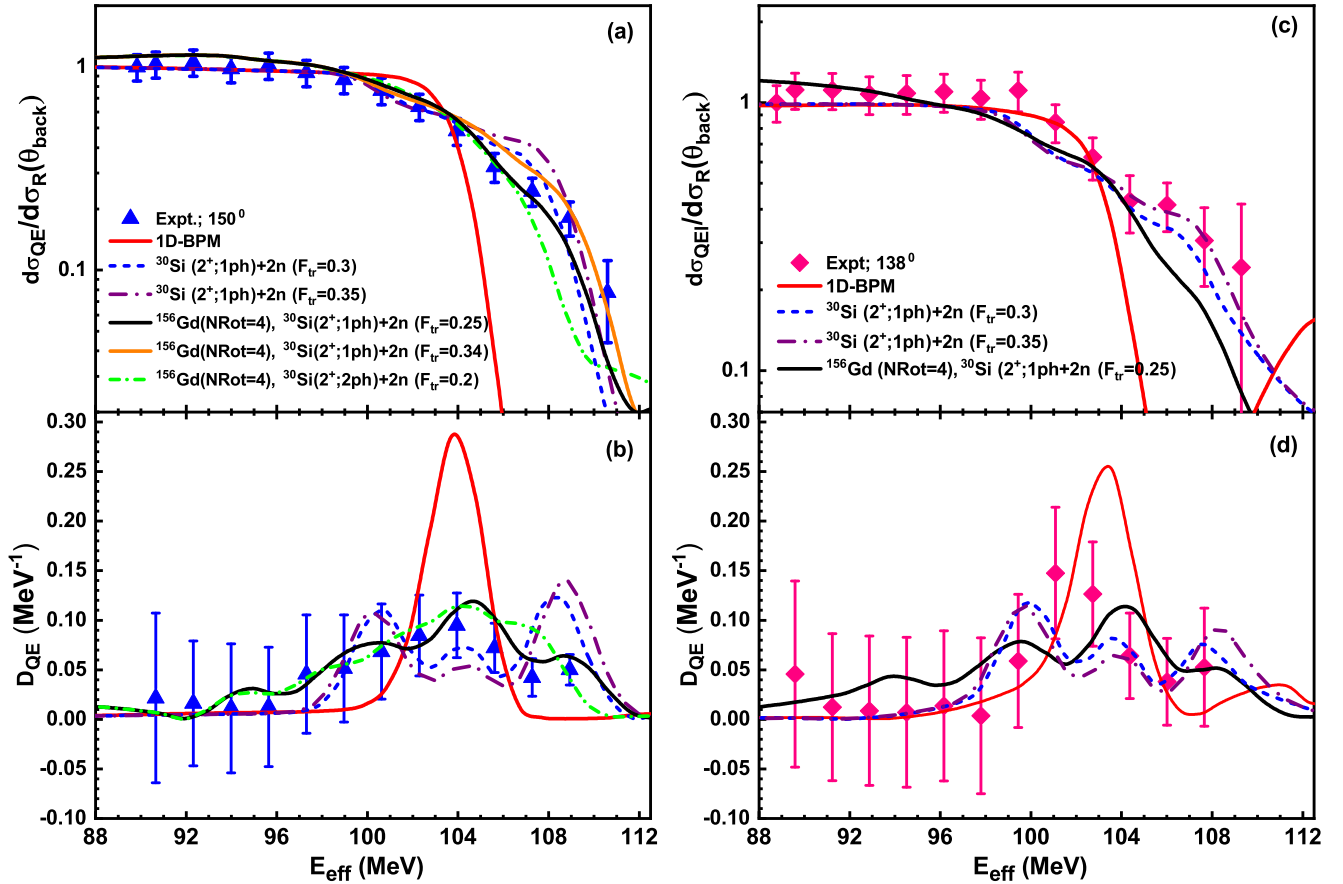
FIG. 10. Comparison between measured data from the ^{30}Si + ^{156}Gd reaction for the QE excitation function and CC calculations with different inelastic coupling options + $2n$-pickup transfer channel alongwith different F_{tr} values using CFULL at (a) $\theta_{lab} = 150°$, (c) $\theta_{lab} = 138°$. Panels (b) and (d) show corresponding barrier distributions.

Furthermore, in the case of $\theta_{lab} = 138°$, EF and D_{QE} are well reproduced (except $E_{eff} = 101$ MeV) by CCFULL predictions when included the inelastic couplings in the projectile (2^+; 1-phonon vibrational state) and positive Q-value $2n$ transfer ($F_{tr} = 0.3$ and 0.35) channel. Furthermore, the collective inelastic channels in p-t nuclei were considered with the $2n$-transfer channel ($F_{tr} = 0.25$) to check the sensitivity of CCFULL predictions. However, these predictions do not explain the QE data and BD in the higher-energy region. Even these predictions are underestimating other theoretical estimations when considering only projectiles' vibrational coupling and the $2n$-transfer channel. The CCFULL predictions considering the IE + $2n$ transfer channel with $F_{tr} = 0.34$ have not been included in the figure as it does not explain the data throughout the studied energy. A quantitative analysis has been presented in the next paragraph using the least-squares deviation analysis.

Least-squares deviation analysis:

A least-squares deviation analysis has been performed for the QE excitation functions at both back angles, which tells about the model predictions to best fit a data set. Suppose that we have n number of measured data points y_i at energy E_i, where $i = 1, 2 \cdots n$ and $f(E_i)$ are the model predicted values of QE excitation functions at energy E_i. Thus, the fit of a model to a data point is measured by the difference between a

measured value and that predicted by the model as

$$\alpha_i = y_i - f(E_i). \tag{9}$$

The least-squares deviation method extracts the optimal parameter values by minimizing the sum of squared deviations $S = \sum_{i=1}^{n} \alpha_i^2$. It can observed from Table IV that when we considered the IEs in interacting nuclei, the sum of squared deviations (S) is least for the 2^+;2ph vibrational state of ^{30}Si and the 2^+;1ph vibrational state of ^{30}Si plus rotational states (up to 8^+) of ^{156}Gd at $\theta_{lab} = 150°$ and $138°$, respectively. However, inclusion of the $2n$-transfer channel with IE, i.e., ^{30}Si (2^+;1ph) + $2n$ ($F_{tr} = 0.35$) and ^{30}Si (2^+;1ph) + $2n$ ($F_{tr} = 0.3$) coupling channels at $\theta_{lab} = 150°$ and $138°$, respectively, provide good fit to the data (least S value). However, it might be pointed out that ^{30}Si (2^+;1ph) + $2n$ ($F_{tr} = 0.35$) channel couplings are also reasonably explaining the data for $138°$, shown in Fig. 10(c).

The barrier distribution from fusion (D_{fus}) has been compared with the corresponding distribution from QE scattering (D_{QE}) at two different back-angles ($\theta_{lab} = 138°$ and $150°$) in Fig. 11. To make a comparison between D_{fus} and D_{QE}, the fusion barrier distribution is normalized by geometrical cross sections πR^2, where $R = 1.2(A_p^{1/3} + A_t^{1/3})$ fm and A_p and A_t are the mass number of projectile and target, respectively. It

TABLE IV. Least-squares deviation analysis of back-angle ($\theta_{\text{lab}} = 150°$ and $138°$) QE scattering excitation functions for the ^{30}Si $+ ^{156}$Gd system.

Figure	Channels	$S^{150°}$	$S^{138°}$
9(a) and 9(c) (IE)	^{30}Si $(2^+;1\text{ph})$	0.203	0.410
	^{30}Si $(2^+;2\text{ph})$	0.123	0.555
	^{156}Gd (NRot=4)	0.195	0.443
	^{156}Gd (NRot=4), ^{30}Si $(2^+;1\text{ph})$	0.130	0.364
10(a) and 10(c) (IE + 2n)	^{30}Si $(2^+;1\text{ph}) + 2n$ ($F_{\text{tr}} = 0.3$)	0.076	0.234
	^{30}Si $(2^+;1\text{ph}) + 2n$ ($F_{\text{tr}} = 0.35$)	0.071	0.246
	^{156}Gd (NRot=4), ^{30}Si $(2^+;1\text{ph}) + 2n$ ($F_{\text{tr}} = 0.25$)	0.094	0.295
	^{156}Gd (NRot=4), ^{30}Si $(2^+;1\text{ph}) + 2n$ ($F_{\text{tr}} = 0.34$)	0.092	
	^{156}Gd (NRot=4), ^{30}Si $(2^+;2\text{ph}) + 2n$ ($F_{\text{tr}} = 0.2$)	0.129	

may be pointed out that D_{fus} and D_{QE} are overall similar in shape within the experimental uncertainties.

E. Potential parameters

In complete fusion reactions, extraction of experimental fusion characteristics, such as barrier height (V_b) and its position (R_b), sheds light on the quality of experimental data. Since one cannot extract these parameters directly from the experiment, it is obtained from the measured fusion cross section of the ^{30}Si $+ ^{156}$Gd system. It is customary to get the simplified classical relation for the fusion cross section from Wong's formula [63] at the energies well above the Coulomb barrier, i.e., $(E_{\text{c.m.}} - V_B) \geqslant \hbar\omega/2\pi$ as shown in Eq. (10).

$$\sigma_{\text{fus}}(E_{\text{c.m.}}) = \pi R_b^2 \left(1 - \frac{V_b}{E_{\text{c.m.}}}\right), \qquad (10)$$

where V_b, R_b, and $\hbar\omega$ are the height, radius, and curvature of the one-dimensional barrier, respectively. The measured fusion cross sections (σ_{fus}) have been plotted against the inverse of center-of-mass energy ($1/E_{\text{c.m.}}$) following Eq. (10), presented in Fig. 12. Here, only the above barrier energy points are considered to obtain the best linear fit through the data to obtain the one-dimensional Coulomb barrier parameters V_b

and R_b using the intercept and slope of the linear fit. The extracted barrier height and radius are 102 ± 3.9 MeV and 9.3 ± 2.3 fm, respectively. The uncertainties in V_b and R_b are obtained from fitting through data. In recent years, efforts have been made to understand the nuclear interactions at a microscopic level because different parametrizations are proposed for the fusion barrier heights and their positions by applying different nuclear potential models, such as prox 2000, prox 2010, Bass 1980, etc. To compare our parameters, theoretical barrier height and radius are estimated using the empirical pocket formulas by Kumari and Puri [59], Zhang and Pan [60], prox 2000, prox 2010 [51,61,62], and Bass 1980 [52] models, listed in Table V. The measured and other theoretical values of V_b and R_b are in close proximity.

F. Comparison with other similar systems

It is essential to compare similar systems to gain insight into the structural peculiarities and the other associated mechanisms with interacting nuclei. The reduced fusion excitation functions of ^{28}Si $+ ^{154}$Sm [10], ^{28}Si $+ ^{144}$Nd [64], ^{32}S $+ ^{154}$Sm [11], ^{60}Ni $+ ^{100}$Mo [19], ^{40}Ca $+ ^{124}$Sn [18], and ^{32}S $+ ^{112,116,120}$Sn [8] have been compared with the present

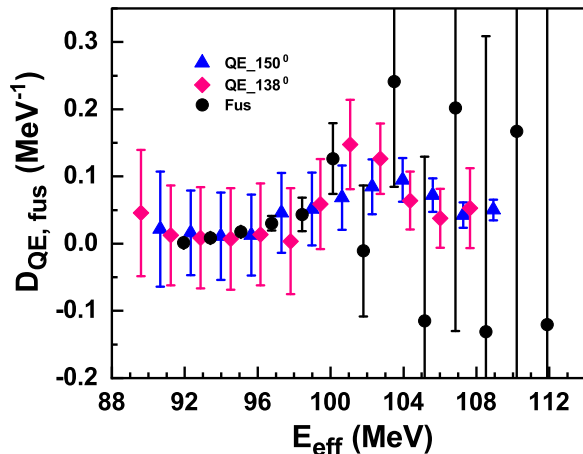FIG. 11. The experimental barrier distributions from fusion and back-angles QE excitation function for the ^{30}Si $+ ^{156}$Gd system.

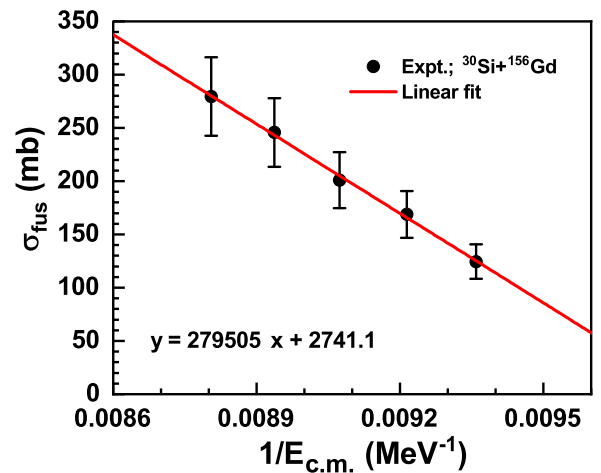FIG. 12. Variation of fusion cross sections (σ_{fus}) of the ^{30}Si $+ ^{156}$Gd system as a function of $1/E_{\text{c.m.}}$. The solid line is a linear fit through the data.

TABLE V. Experimentally extracted and theoretically [51,52,59–62] estimated nuclear potential parameters for the ^{30}Si + ^{156}Gd reaction.

Method	V_b (MeV)	R_b (fm)
Experiment	102 ± 3.9	9.3 ± 2.3
Kumari *et al.*	102.2	11.1
Zhang *et al.*	103.8	11.5
Prox 2000	105.4	11.4
Prox 2010	105.9	11.4
Bass 80	104.8	11.5

measurements, which are populating the compound nucleus in the mass range of 144–186, having positive and negative Q-value neutron transfer channels, shown in Fig. 13(a). To make the comparison more apparent, fusion cross sections (σ_{fus}) and $E_{c.m.}$ are scaled by the respective geometrical cross section (πR^2) and Bass-barrier height (V_b), respectively. In transfer reactions, certain kinematical conditions including Q-value systematics should be satisfied to achieve the large transfer probability. As per Jiang *et al.* [20], excitation energy in the outgoing channel, i.e., $E_x^* \approx Q_{gg} - (V_b^f - V_b^i)$, where Q_{gg}, $V_b^{i,f}$ are the ground-state Q values, Coulomb barrier in the entrance or exit channel, respectively, should be positive for nucleon transfer as the negative values are energetically forbidden. Thus, in later cases transfer cross sections should have small contribution in sub-barrier fusion enhancement. The E_x^* resulting from one to six neutron transfers for all the systems are presented in Fig. 13(b).

It can be observed from Fig. 13(a), the ^{40}Ca + ^{124}Sn, ^{32}S + ^{112,116,120}Sn, and ^{30}Si + ^{156}Gd systems, with positive excitation energies for the 2n-pickup channel, show almost similar behavior. However, no additional sub-barrier fusion enhancement was observed in ^{32}S + ^{112,116}Sn reactions despite having positive excitation energy for 2n transfer, which is a similar conclusion as the present paper. Although for ^{40}Ca + ^{124}Sn, ^{60}Ni + ^{100}Mo, and ^{28}Si + ^{144}Nd systems, a correlation between the sub-barrier fusion and the positive excitation energy for neutron transfer channels has been reported.

Apart from the negative excitation energies for multi n-pickup (except 2n-pickup transfer) channels, the present system also has negative E_x^* for n-stripping channels up to 6n, indicating the insignificant role of n-stripping channels in sub-barrier fusion cross section enhancement. Also, Q values (or E*) for 1p pickup and stripping channels are negative. In contrast, 2p pickup and stripping channels have $+1.5$ MeV (E*$=-9.9$ MeV) and -11.5 MeV (E*$=+0.8$ MeV), respectively, whose contribution may depend upon the optimum Q value of the reaction. Besides, it may be noted that the reduced fusion excitation functions for the ^{28}Si + ^{154}Sm and ^{32}S + ^{154}Sm systems are significantly enhanced as compared to other systems in the sub-barrier region. This enhancement may be primarily due to the deformed target (^{154}Sm) and the weak effect of positive excitation energy for multinucleon transfer channels [see Fig. 13(b)].

Moreover, according to Sargsyan *et al.* [26], the systems which have $+Q_{2n}$ (positive excitation energy) should show an enhancement in sub-barrier fusion if the deformation (β_2) of colliding nuclei increases, and the mass asymmetry of the system decreases after 2n transfer. The increment in
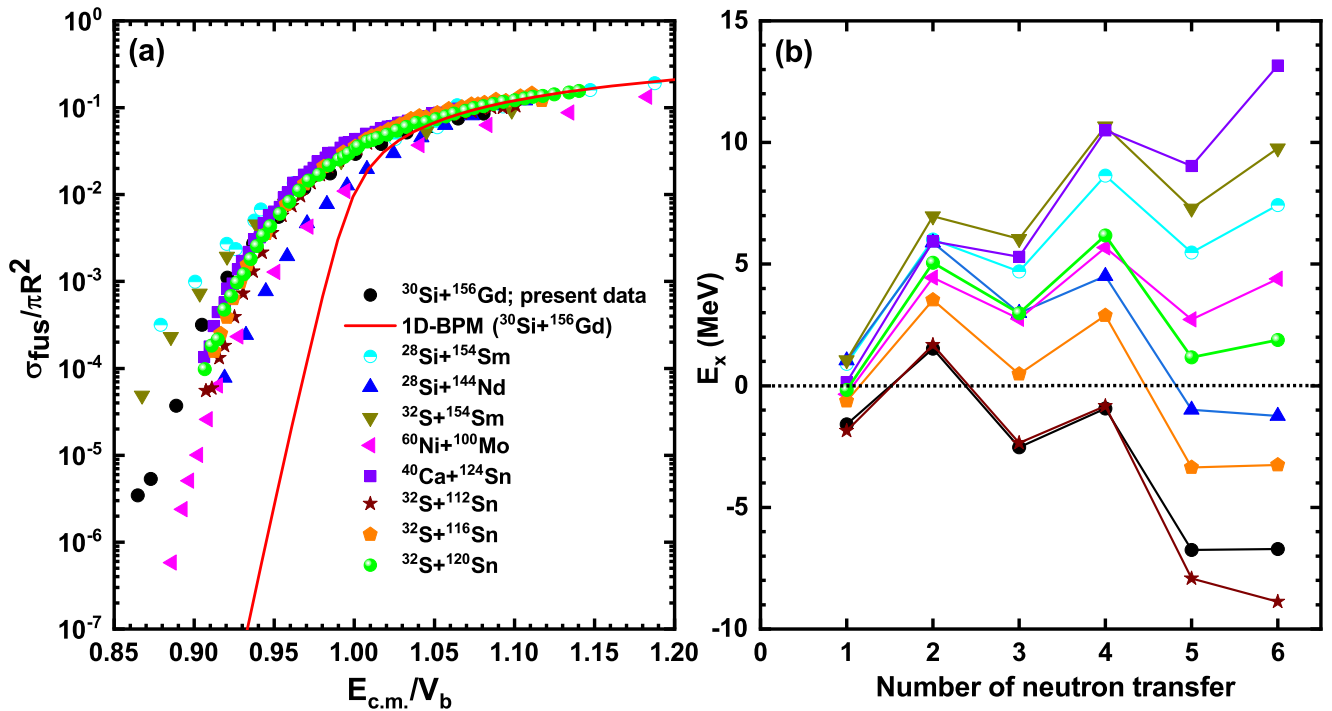

FIG. 13. (a) Reduced fusion excitation functions for the present system ^{30}Si + ^{156}Gd compared with other similar systems having positive and negative Q values for the 2n-transfer channel and (b) excitation energies of neutron pickup reactions for the same systems. Fusion data for the comparison have been taken from the literature referenced in the text.

TABLE VI. The quadrupole deformation (β_2) [53,65] of different projectile-target nuclei and mass-asymmetries (η) of systems before and after 2n-pickup transfer. The listed systems are used for comparison in Fig. 13.

Systems	Before 2n transfer		After 2n transfer	
	β_2	η	β_2	η
^{30}Si + ^{156}Gd	^{30}Si (-0.236) + ^{156}Gd (0.26)	0.68	^{32}Si (-0.124) + ^{154}Gd (0.237)	0.66
^{28}Si + ^{154}Sm	^{28}Si (-0.363) + ^{154}Sm (0.341)	0.69	^{30}Si (-0.236) + ^{152}Sm (0.3064)	0.67
^{28}Si + ^{144}Nd	^{28}Si (-0.363) + ^{144}Nd (0.1237)	0.67	^{30}Si (-0.236) + ^{142}Nd (0.0917)	0.65
^{32}S + ^{154}Sm	^{32}S (0.312) + ^{154}Sm (0.341)	0.66	^{34}S (0.252) + ^{152}Sm (0.3064)	0.65
^{60}Ni + ^{100}Mo	^{60}Ni (0.207) + ^{100}Mo (0.231)	0.25	^{62}Ni (0.1978) + ^{98}Mo (0.1683)	0.23
^{40}Ca + ^{124}Sn	^{40}Ca (0.123) + ^{124}Sn (0.0953)	0.51	^{42}Ca (0.247) + ^{122}Sn (0.1036)	0.49
^{32}S + ^{112}Sn	^{32}S (0.312) + ^{112}Sn (0.1226)	0.56	^{34}S (0.252) + ^{110}Sn (0.120)	0.53
^{32}S + ^{116}Sn	^{32}S (0.312) + ^{116}Sn (0.1118)	0.57	^{34}S (0.252) + ^{114}Sn (0.121)	0.54
^{32}S + ^{120}Sn	^{32}S (0.312) + ^{120}Sn (0.1075)	0.58	^{34}S (0.252) + ^{118}Sn (0.1105)	0.55

deformation of interacting nuclei leads to the reduction in barrier height, resulting in a higher fusion cross section. However, neutron transfer weakly influences the fusion cross section if deformations of nuclei do not change or slightly decrease. The quadrupole deformation (β_2) of nuclei and mass-asymmetry ($\eta = \frac{A_t - A_p}{A_t + A_p}$; A_p and A_t are the mass number of projectile and target, respectively) of systems before and after the 2n transfer are listed in Table VI. It can be observed from this table that for the ^{28}Si + ^{154}Sm, and ^{32}S + ^{154}Sm systems deformation is substantially decreasing after 2n transfer; hence, enhancement at sub-barrier energies in the underlying reactions may not be related to the transfer, but it is due to a highly deformed target as also mentioned previously. Moreover, mass asymmetry of all the systems decreases after the 2n transfer. Similarly, weak dependence of neutron transfer effect on the sub-barrier fusion cross section is expected in the ^{28}Si + ^{144}Nd and ^{60}Ni + ^{100}Mo systems where the deformations slightly decrease and/or do not change much. However, a considerable enhancement was reported in the ^{40}Ca + ^{124}Sn and ^{32}S + ^{120}Sn systems at sub-barrier energies, which can be understood based on increasing deformations after 2n transfer. Whereas it can be seen that the deformation in ^{32}S + ^{112,116}Sn and ^{30}Si + ^{156}Gd (present paper) systems is decreasing, and no significant effect of PQNT has been reported and observed, respectively. Therefore, the present analysis is also in agreement with the reported data by Tripathi *et al.* [8] and systematics made by Sargsyan *et al.* [26].

IV. CONCLUSION

This article reports the measurement of fusion and back-angle QE scattering excitation functions of the system ^{30}Si + ^{156}Gd covering a wide range of incident beam energies around the Coulomb barrier. The measured data have been analyzed within the framework of coupled channel predictions using CCFULL and ECC model codes. Sub-barrier fusion enhancement over 1D-BPM has been explained by considering the couplings to low-energy inelastic modes of colliding nuclei, particularly, rotational excitations of the target nucleus played a vital role in CCFULL calculations. Since the system has a positive Q value for the 2n-pickup channel, the transfer channel and inelastic excitation couplings are examined using the above model codes. Inclusion of the 2n-transfer channel and collective excitations improves the fit to the experimental fusion data and subsequent BD in a short span of energy window around the Coulomb barrier, whereas no significant effect has been observed at the sub-barrier region using the CCFULL program. Furthermore, no such effect of 2n transfer with a positive Q value has been observed in the ECC model calculations. In contrast, both model codes explain the measured data quite successfully using collective modes in colliding nuclei only. This difference in the role of 2n transfer may be due to the consideration of different model approaches, such as quantum coupled channel and semiclassical in CCFULL and ECC models, respectively. Thus, no conclusion can be drawn on the role of the positive Q-value 2n-transfer effect on sub-barrier fusion cross sections as the uncertainty witnessed by two different models in the present studies.

Measured back-angle ($\theta_{\text{lab}} = 138°$, $150°$) QE excitation functions and corresponding BDs are grossly explained by CC calculations considering the collective excitations with 2n-transfer channel couplings in interacting partners using the CCFULL program. Fusion and QE BDs are found to be almost similar in shape within the experimental uncertainty. Also, one-dimensional barrier parameters extracted from the measured data are in good agreement with the theoretical models.

Moreover, it would be appropriate to comment that more dedicated experiments and CC calculations with the accurate transfer couplings are required to unravel the effect of positive Q-value neutron transfer in sub-barrier fusion and understand the associated physics of heavy-ion reactions.

[1] M. La Commara, J. Gómez del Campo, A. D'Onofrio, A. Gadea, M. Glogowski, P. Jarillo-Herrero, N. Belcari, R. Borcea, G. de Angelis, C. Fahlander *et al.*, Nucl. Phys. A **669**, 43 (2000).

[2] Y. X. Watanabe, Y. H. Kim, S. C. Jeong, Y. Hirayama, N. Imai, H. Ishiyama, H. S. Jung, H. Miyatake, S. Choi, J. S. Song *et al.*, Phys. Rev. Lett. **115**, 172503 (2015).

[3] G. Wallerstein, I. Iben, Jr., P. Parker, A. M. Boesgaard, G. M. Hale, A. E. Champagne, C. A. Barnes, F. Käppeler, V. V. Smith, R. D. Hoffman *et al.*, Rev. Mod. Phys. **69**, 995 (1997).

[4] C. L. Jiang, B. B. Back, K. E. Rehm, K. Hagino, G. Montagnoli, and A. M. Stefanini, Eur. Phys. J. A **57**, 235 (2021).

[5] B. B. Back, H. Esbensen, C. L. Jiang, and K. E. Rehm, Rev. Mod. Phys. **86**, 317 (2014).

[6] M. Beckerman, Rep. Prog. Phys. **51**, 1047 (1988).

[7] M. Dasgupta, D. J. Hinde, N. Rowley, and A. M. Stefanini, Annu. Rev. Nucl. Part. Sci. **48**, 401 (1998).

[8] V. Tripathi, L. T. Baby, J. J. Das, P. Sugathan, N. Madhavan, A. K. Sinha, P. V. Madhusudhana Rao, S. K. Hui, R. Singh, and K. Hagino, Phys. Rev. C **65**, 014614 (2001).

[9] A. Chauhan, R. Prajapat, G. Sarkar, M. Maiti, R. Kumar, Malvika, Gonika, J. Gehlot, S. Nath, A. Parihari, and N. Madhavan, Phys. Rev. C **102**, 064606 (2020).

[10] S. Gil, D. Abriola, D. E. DiGregorio, M. di Tada, M. Elgue, A. Etchegoyen, M. C. Etchegoyen, J. Fernández Niello, A. M. J. Ferrero, A. O. Macchiavelli *et al.*, Phys. Rev. Lett. **65**, 3100 (1990).

[11] P. R. S. Gomes, I. C. Charret, R. Wanis, G. M. Sigaud, V. R. Vanin, R. Liguori Neto, D. Abriola, O. A. Capurro, D. E. DiGregorio, M. di Tada *et al.*, Phys. Rev. C **49**, 245 (1994).

[12] Khushboo, N. Madhavan, S. Nath, A. Jhingan, J. Gehlot, B. Behera, S. Verma, S. Kalkal, and S. Mandal, Phys. Rev. C **100**, 064612 (2019).

[13] N. K. Deb, K. Kalita, H. A. Rashid, S. Nath, J. Gehlot, N. Madhavan, R. Biswas, R. N. Sahoo, P. K. Giri, A. Das *et al.*, Phys. Rev. C **102**, 034603 (2020).

[14] S. Kalkal, S. Mandal, N. Madhavan, E. Prasad, S. Verma, A. Jhingan, R. Sandal, S. Nath, J. Gehlot, B. R. Behera *et al.*, Phys. Rev. C **81**, 044610 (2010).

[15] V. I. Zagrebaev, V. V. Samarin, and W. Greiner, Phys. Rev. C **75**, 035809 (2007).

[16] V. I. Zagrebaev and V. V. Samarin, Phys. Atom. Nucl. **67**, 1462 (2004).

[17] V. I. Zagrebaev, Phys. Rev. C **64**, 034606 (2001); **67**, 061601(R) (2003).

[18] F. Scarlassara, S. Beghini, G. Montagnoli, G. F. Segato, D. Ackermann, L. Corradi, C. J. Lin, A. M. Stefanini, and L. F. Zheng, Nucl. Phys. A **672**, 99 (2000).

[19] A. M. Stefanini, G. Montagnoli, F. Scarlassara, C. L. Jiang, H. Esbensen, E. Fioretto, L. Corradi, B. B. Back, C. M. Deibel, and B. Di Giovine, Eur. Phys. J. A **49**, 63 (2013).

[20] C. L. Jiang, K. E. Rehm, B. B. Back, H. Esbensen, R. V. F. Janssens, A. M. Stefanini, and G. Montagnoli, Phys. Rev. C **89**, 051603(R) (2014).

[21] R. Vandenbosch, A. A. Sonzogni, and J. D. Bierman, J. Phys. G: Nucl. Part. Phys. **23**, 1303 (1997).

[22] J. J. Kolata, A. Roberts, A. M. Howard, D. Shapira, J. F. Liang, C. J. Gross, R. L. Varner, Z. Kohley, A. N. Villano, H. Amro *et al.*, Phys. Rev. C **85**, 054603 (2012).

[23] W. Henning, F. L. H. Wolfs, J. P. Schiffer, and K. E. Rehm, Phys. Rev. Lett. **58**, 318 (1987).

[24] Z. Kohley, J. F. Liang, D. Shapira, R. L. Varner, C. J. Gross, J. M. Allmond, A. L. Caraley, E. A. Coello, F. Favela, K. Lagergren *et al.*, Phys. Rev. Lett. **107**, 202701 (2011).

[25] H. M. Jia, C. J. Lin, F. Yang, X. X. Xu, H. Q. Zhang, Z. H. Liu, L. Yang, S. T. Zhang, P. F. Bao, and L. J. Sun, Phys. Rev. C **86**, 044621 (2012).

[26] V. V. Sargsyan, G. G. Adamian, N. V. Antonenko, W. Scheid, and H. Q. Zhang, Phys. Rev. C **85**, 024616 (2012).

[27] H. Timmers, J. R. Leigh, M. Dasgupta, D. J. Hinde, R. C. Lemmon, J. C. Mein, C. R. Morton, J. O. Newton, and N. Rowley, Nucl. Phys. A **584**, 190 (1995).

[28] E. Piasecki, Ł. Świderski, N. Keeley, M. Kisieliński, M. Kowalczyk, S. Khlebnikov, T. Krogulski, K. Piasecki, G. Tiourin, M. Sillanpää *et al.*, Phys. Rev. C **85**, 054608 (2012).

[29] O. A. Capurro, J. E. Testoni, D. Abriola, D. E. DiGregorio, G. V. Martí, A. J. Pacheco, and M. R. Spinella, Phys. Rev. C **61**, 037603 (2000).

[30] H. M. Jia, C. J. Lin, F. Yang, X. X. Xu, H. Q. Zhang, Z. H. Liu, Z. D. Wu, L. Yang, N. R. Ma, P. F. Bao, and L. J. Sun, Phys. Rev. C **90**, 031601(R) (2014).

[31] Y. K. Gupta, B. K. Nayak, U. Garg, K. Hagino, K. B. Howard, N. Sensharma, M. Şenyiğit, W. P. Tan, P. D. O'Malley, M. Smith *et al.*, Phys. Lett. B **806**, 135473 (2020).

[32] T. Tanaka, K. Morita, K. Morimoto, D. Kaji, H. Haba, R. A. Boll, N. T. Brewer, S. Van Cleve, D. J. Dean, S. Ishizawa *et al.*, Phys. Rev. Lett. **124**, 052502 (2020).

[33] S. Mitsuoka, H. Ikezoe, K. Nishio, K. Tsuruta, S. C. Jeong, and Y. Watanabe, Phys. Rev. Lett. **99**, 182701 (2007).

[34] R. Prajapat, M. Maiti, D. Kumar, and A. Chauhan, Phys. Scr. **95**, 055306 (2020).

[35] D. Kumar, M. Maiti, and S. Lahiri, Phys. Rev. C **94**, 044603 (2016).

[36] R. Prajapat and M. Maiti, Phys. Rev. C **101**, 064620 (2020).

[37] R. Prajapat and M. Maiti, Phys. Rev. C **101**, 024608 (2020).

[38] R. Prajapat and M. Maiti, Phys. Rev. C **103**, 034620 (2021).

[39] R. Kumar, M. Maiti, T. N. Nag, and S. Sodaye, Phys. Rev. C **104**, 064606 (2021).

[40] D. Kumar, M. Maiti, and S. Lahiri, Phys. Rev. C **96**, 014617 (2017).

[41] R. Prajapat, M. Maiti, and D. Kumar, Phys. Rev. C **103**, 014608 (2021).

[42] P. Kaur, M. Maiti, T. N. Nag, and S. Sodaye, Phys. Rev. C **105**, 014629 (2022).

[43] R. Prajapat, M. Maiti, S. R. Abhilash, G. R. Umapathy, D. Kabiraj, S. A. Khan, D. Khandelwal, and A. Dawar, Vacuum **201**, 111033 (2022).

[44] J. F. Ziegler, M. D. Ziegler, and J. P. Biersack, Nucl. Instrum. Methods Phys. Res. B **268**, 1818 (2010).

[45] A. K. Sinha, N. Madhavan, J. J. Das, P. Sugathan, D. O. Kataria, A. P. Patro, and G. K. Mehta, Nucl. Instrum. Methods Phys. Res., Sect. A **339**, 543 (1994).

[46] E. T. Subramaniam, B. P. Ajith Kumar, and R. K. Bhowmik, Collection and analysis of nuclear data using linux network (unpublished).

[47] A. Gavron, Phys. Rev. C **21**, 230 (1980).

[48] S. Nath, Comput. Phys. Commun. **179**, 492 (2008); **180**, 2392 (2009).

[49] S. Nath, P. V. M. Rao, S. Pal, J. Gehlot, E. Prasad, G. Mohanto, S. Kalkal, J. Sadhukhan, P. D. Shidling, K. S. Golda *et al.*, Phys. Rev. C **81**, 064601 (2010).

[50] K. Hagino, N. Rowley, and T. Kruppa, Comput. Phys. Commun. **123**, 143 (1999).

[51] I. Dutt and R. K. Puri, Phys. Rev. C **81**, 064608 (2010); **81**, 064609 (2010).

[52] R. Bass, Phys. Rev. Lett. **39**, 265 (1977).

[53] P. Möller, A. J. Sierk, T. Ichikawa, and H. Sagawa, At. Data Nucl. Data Tables **109-110**, 1 (2016).

[54] T. Kibedi and R. H. Spear, At. Data Nucl. Data Tables **80**, 35 (2002).

[55] C. H. Dasso and G. Pollarolo, Phys. Lett. B **155**, 223 (1985); C. H. Dasso and A. Vitturi, *ibid.* **179**, 337 (1986).

[56] H. Timmers, D. Ackermann, S. Beghini, L. Corradi, J. H. He, G. Montagnoli, F. Scarlassara, A. M. Stefanini, and N. Rowley, Nucl. Phys. A **633**, 421 (1998).

[57] S. Biswas, A. Chakraborty, A. Jhingan, D. Arora, B. R. Behera, R. Biswas, N. K. Deb, S. S. Ghugre, P. K. Giri, K. S. Golda *et al.*, Phys. Rev. C **102**, 014613 (2020).

[58] G. Kaur, B. R. Behera, A. Jhingan, B. K. Nayak, R. Dubey, P. Sharma, M. Thakur, R. Mahajan, N. Saneesh, T. Banerjee *et al.*, Phys. Rev. C **94**, 034613 (2016).

[59] R. Kumari and R. K. Puri, Nucl. Phys. A **933**, 135 (2015).

[60] G. L. Zhang and M. Pan, Int. J. Mod. Phys. E **25**, 1650082 (2016).

[61] R. Gharaei and G. L. Zhang, Nucl. Phys. A **990**, 294 (2019).

[62] O. N. Ghodsi and F. Lari, Mod. Phys. Lett. A **28**, 1350116 (2013).

[63] C. Y. Wong, Phys. Rev. Lett. **31**, 766 (1973).

[64] A. K. Sinha, L. T. Baby, N. Badiger, J. J. Das, S. K. Hui, D. O. Katari, R. G. Kulkarni, N. Madhavan, P. V. Madhusudhana Rao, I. Majumdar *et al.*, J. Phys. G: Nucl. Part. Phys. **23**, 1331 (1997).

[65] S. Raman, C. W. Nestor, Jr., and P. Tikkanen, At. Data Nucl. Data Tables **78**, 1 (2001).